# Chapter 1

# Uncertainty Quantification Applied to Aeroacoustics of Wall-Bounded Flows

Julien Christophe*, Marlène Sanjose†, Jeroen Witteveen‡ and Stéphane Moreau†

*Institut von Karman, 72 Chaussée de Waterloo B-1640 Rhode-Saint-Genese, Belgium, julien.jchristophe@vki.ac.be

†Université de Sherbrooke, 2500 boulevard de l'université Sherbrooke, QC, Canada, J1K2R1

‡Center for Mathematics and Computer Science (CWI) Amsterdam, The Netherlands

The uncertainty quantification (UQ) related to the self-noise prediction based on a Reynolds-Averaged Navier-Stokes (RANS) flow computation of a low-subsonic axial fan has been achieved. As the methodology used for fan noise prediction is based on airfoil theories, the uncertainty quantification of a low-speed Controlled-Diffusion (CD) airfoil has been first considered. For both applications, deterministic incompressible flow solvers are coupled with a non-intrusive stochastic collocation method, found to be two orders-of-magnitude more efficient than a classical Monte Carlo simulation for the same accuracy. In the case of airfoil UQ, the effective flow angle is used as a random variable. Two wall-pressure reconstruction models are used to obtain necessary inputs of Amiet's trailing-edge noise model: Rozenberg's model has larger uncertainties at high frequencies because of the uncertainty on the wall-shear stress parameter required in the method, and Panton & Linebarger's model is less accurate at low frequencies because of the slow statistical convergence of the integration involved in the model. Similar behaviours are observed in the fan UQ involving the volume flow-rate and the rotational speed as random variables. The stochastic mean sound spectra are found to

be dominated by the tip strip and compare well with experimental data. Larger uncertainties are seen in the hub and tip regions, where large flow detachment and recirculation appear. The known uncertainties on flow rate yield larger uncertainties on sound than those on rotational speed.

## 1. Introduction

In modern rotating machines, significant effort has been put to reduce annoying tonal noise, either by passive devices or by active noise control. The next challenge is then to reduce the broadband contribution to decrease the overall noise level and meet increasingly stringent environmental noise regulations. A key source of broadband noise is the trailing-edge noise or self-noise, caused by the scattering of boundary-layer pressure fluctuations into acoustic waves at the trailing edge of any lifting surface. In the absence of any interaction noise source, it represents the dominant source of noise generated by rotating machines such as low-speed fans, high-speed turboengines,[1] wind turbines[2] and other high-lift devices.[3] However, an accurate prediction of the sound by a rotating system still remains a daunting task by a direct computation (a compressible Large Eddy Simulation (LES) for instance). A hybrid approach combining a near-field turbulent flow simulation and an acoustic analogy for the sound propagation in the far-field is therefore preferred. Such a method has been thoroughly validated for broadband noise prediction on multiple airfoils in various flow conditions including blowing.[4–13] The computational cost associated with unsteady turbulent flow simulations still limits most numerical studies to simpler geometries such as airfoils,[8] even with sophisticated non-boundary-conforming methods such as the Lattice Boltzmann method and Immersed Boundary method,[4,14] or the use of unstructured grid topologies.[5] To meet industrial design constraints of rotating machines, approaches that model the pressure and velocity fluctuations needed for an acoustic analogy from steady RANS are often used.[15–18] These methods add further levels of modeling and the associated uncertainties grow, which may make the final acoustic prediction of fan broadband self-noise inaccurate and unreliable.

To illustrate this point, some of the aleatory uncertainties associated with the prediction of trailing-edge noise are considered, first for the wall-bounded canonical case of airfoil noise as measured in an open-jet wind tunnel,[6,19] and then for the actual complex case of a low-speed automotive engine cooling fan as tested in a reverberant wind tunnel.[20] For the former the uncertainty propagation from uncertain inlet velocity profiles caused by

inaccurate knowledge of the jet deflection induced by the airfoil is studied. For the latter the uncertainty propagation from uncertain operating conditions (both volume flow-rate through the fan and rotational speed) mainly caused by industrial process issues is considered. In doing so, two representative wall-pressure models derived from steady RANS are dealt with, and compared with direct unsteady LES predictions of the trailing-edge noise for the airfoil case. The sensitivity of the RANS and LES solutions to inlet conditions and the uncertainty introduced by wall-pressure models coupled with RANS on the prediction of the noise sources and the far-field pressure are then assessed. The difference is made here between uncertainties in the physical inputs to the problem (aleatoric uncertainties) and the constants or variables of the model used to solve for the flow, for instance all constants used in the turbulence modeling, or for the far-field noise (epistemic uncertainties).[21]

The methodology for uncertainty quantification based on simulations of either a standard experimental setup for trailing-edge airfoil noise or a wall-mounted fan in a standard interface is presented in Sec. 2. The present stochastic approach is outlined in Sec. 3. The sound prediction methods are then presented in Sec. 4. The next two sections, Secs. 5 and 6, show the uncertainty quantification for the airfoil and the fan cases respectively. For both examples the deterministic flow simulations are briefly outlined, the random variables are described, and the stochastic aerodynamic and acoustic results are compared with the available experimental data. Conclusions are finally drawn in Sec. 7.

## 2. Uncertainty Quantification Methodology

The methods involved in the fan noise prediction rely on airfoil aeroacoustic models,[22] and the uncertainty related to such models is first assessed. The approaches to compute airfoil or fan trailing-edge noise are illustrated in Fig. 1.1. The directions of the arrows outline the logical sequence of the method. Starting from the fan blade geometry (grey square box), two different methodologies based on similar computational methods are used to study trailing-edge noise in the case of airfoil or fan applications.

On the one hand, a mid-span cut of an automotive cooling fan is performed to obtain a two-dimensional profile, and used to study uncertainty for airfoil trailing-edge noise. As in previous studies[4–13] the same validated numerical method for predicting trailing-edge noise is used. A computation of the complete experimental setup of the large anechoic wind tunnel

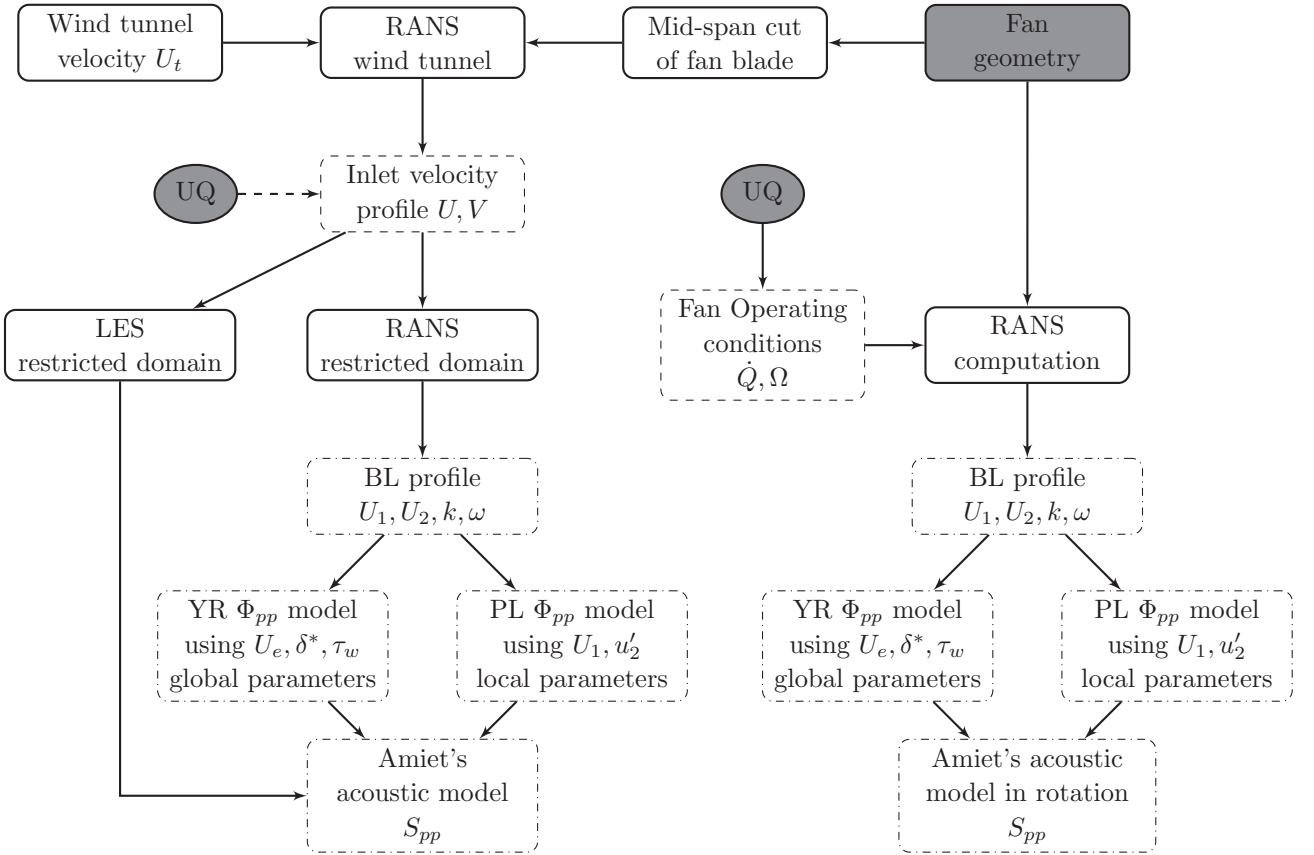


Fig. 1.1. Uncertainty quantification methodology: the solid-line rectangular boxes refer to the different computational steps in the hybrid methodology, the dashed-line rectangular boxes denote the main inputs and the dash-dotted-line boxes denote the outputs at each step and the arrows indicate the various possible workflows to yield the final acoustic pressure. The round box refers to the point where uncertainty quantification is introduced.

in Ecole Centrale de Lyon (LWT), including the nozzle and part of the anechoic chamber is first done in order to capture the strong jet-airfoil interaction and its impact on airfoil loading.[23] The input parameters for this computation, termed "wind tunnel" in Fig. 1.1, are the wind tunnel velocity $U_t$, air density $\rho$, and kinematic viscosity $\nu$. The computational setup, defined by the nozzle and the airfoil geometries as well as the position of the airfoil in the wind tunnel and its geometrical angle of attack $\alpha_w$ with respect to the nozzle axis,[23] is directly taken from measurements on the experimental setup, and is therefore considered as a minor source of possible error on the final sound prediction results. Similarly, the uncertainty on the air density $\rho$ and kinematic viscosity $\nu$, obtained from the experiments ambient conditions, are also neglected. Once a value for the wind tunnel velocity $U_t$ is selected, a RANS computation is run on the complete setup and boundary conditions are extracted ($U$ and $V$ profiles) for a smaller domain, termed "restricted domain" in Fig. 1.1, embedded in the jet potential core as shown in Fig. 1.2(a). The final sound prediction is obtained by two different procedures, both producing a wall-pressure frequency spectrum $\Phi_{pp}$ used in Amiet's theory to predict the far-field sound spectrum $S_{pp}$. In the first approach, which is simpler and more intuitive but also more computationally expensive, an unsteady LES on the restricted domain with the steady velocity profiles extracted from RANS is used to obtain a direct prediction of the trailing-edge wall-pressure spectrum. In the clean inflow of the jet potential core, no perturbations are introduced at the inlet of the computational domain. The second approach, which is less expensive but requires more modelling, uses steady RANS computations on a two-dimensional slice of the restricted domain, with the same boundary condition profiles as for the LES. From this RANS computation, the primitive variables ($U_1$ and $U_2$, velocity components parallel and perpendicular to the wall surface respectively, and $k$ and $\omega$ or $\epsilon$ depending on the RANS turbulence model) are extracted through a boundary-layer profile at the trailing edge of the airfoil. Those variables are then used in the two wall-pressure models investigated in the present study. The first model is that of Rozenberg *et al.*[17] (termed YR), who proposed a model only based on global boundary-layer parameters from the boundary-layer profile, namely the external velocity $U_e$, a boundary-layer thickness $\delta$ or instead the displacement thickness $\delta^*$, and the wall shear stress $\tau_w$. The second model by Panton & Linebarger[24] (termed PL) uses local parameters i.e. the wall parallel velocity profile $U_1(y)$ and the wall perpendicular velocity fluctuation profile $u_2'(y)$. For validation purposes, LES output quantities would be

also used in the wall-pressure models, as illustrated in a previous study.[18] The uncertainty is introduced in both velocity components ($U$ and $V$), as shown in Fig. 1.1 by the $UQ$ box, correlated via the non-uniform inlet flow angle at the inlet boundary condition on the restricted computational domain as described in Sec. 5. It not only represents the actual experimental uncertainty but also the uncertainty in the prediction of the flow deflection induced by the airfoil-jet interaction by various turbulence models in the RANS simulation of the whole wind tunnel.[23] The introduction of uncertainty is investigated through approaches, using LES to directly obtain the trailing-edge wall-pressure spectrum and using RANS and wall-pressure spectrum models. A direct comparison of all the methods of prediction of wall-pressure spectrum can then be achieved in terms of mean values and uncertainty bars. These uncertainty bars refer to the numerical results (either RANS or LES) only, and they come from the propagation of all the considered uncertainty introduced on the inlet velocity components to the final aerodynamic and aeroacoustic numerical predictions. When possible, the different steps of the methodology are compared with available experimental measurements and the RANS intermediate results are compared with data obtained directly from the LES. Other possibilities to introduce uncertainty, not shown in Fig. 1.1 and not applied in the present work, would be to perturb the wind tunnel velocity $U_t$ used in the computation of the complete wind tunnel setup, leading to negligible effects on the far-field sound spectrum, or on the boundary-layer parameters used in the wall-pressure reconstruction models, which does not allow a direct comparison between LES and RANS prediction methods.

On the other hand, the approach to UQ to compute fan trailing-edge noise is also illustrated in Fig. 1.1. As in Christophe *et al.*,[25] a RANS computation of flow in a blade passage of the fan is first performed. The input parameters for this computation are the volume flow rate $\dot{Q}$ and the rotational speed $\Omega$. Both parameters are considered as main parameters for the uncertainty quantification on fan operating conditions (solid circle in Fig. 1.1). These uncertainties actually correspond to the dispersion found in engine cooling modules induced by the process scattering of electrical motors (scatter in rotational speed) and heat exchangers (scatter in flow rate). In a blade-to-blade plane at a given radius, the speed triangles yield similar velocity components as in the airfoil case, which relate both uncertainty quantification studies. The computational setup, defined by the fan and tip gap are directly taken from the design of the experimental setup, and is therefore considered as a minor source of possible error on the final

sound prediction results. From this RANS computation, the primitive variables are extracted through a boundary-layer profile at the trailing-edge of the fan blade, at five radial positions along the blade span. Those variables are then used to reconstruct wall-pressure fluctuation spectra $\Phi_{pp}$, using similar reconstructions methods as for the airfoil application. Finally, the latter power spectral densities provide the far-field sound spectrum $S_{pp}$ in the extended Amiet's theory,[26] applied in rotation as explained below in Sec. 4.

## 3. Stochastic Method

Classical methods for stochastic differential equations rely on Monte Carlo (MC) simulations that prescribe ensemble random inputs to these equations and then collect their ensemble solution realizations. They only require running a deterministic solver repetitively and do not depend strongly on the stochastic dimensionality of the problem; however, they suffer from a slow convergence rate and require a large number of samples, which is prohibitive for turbulent flow realizations. An example of this method is presented below in the airfoil case. Alternative methods are sensitivity methods based on the moments, perturbation methods where all stochastic variables are expanded in Taylor expansions around their mean,[27,28] stochastic collocation methods, and spectral or Galerkin projection methods.[29–31] The first two methods either strongly depend on the modeling assumptions or are limited to small variations. As existing flow solvers are used, non-intrusive stochastic methods are preferred, which means that projection is not applied to the Navier-Stokes equations directly, but rather to its inputs and outputs. Among the various projection methods, the Stochastic Collocation expansion (SC) is selected as it has proved its efficiency for flow simulations in various regimes.[32–34]

In this framework[32–34] the vector of random input parameters is given by $\vec{\xi} \in \Xi$, with $\Xi$ the underlying parameter space and probability density $f_\xi(\vec{\xi})$. The objective of UQ is to compute the probability distribution and the moments $\mu_{\mathrm{X}_i}$ of output of interest $X(\vec{\xi})$ defined as

$$\mu_{X_i} = \int_\Xi X(\vec{\xi})^i f_\xi(\vec{\xi}) \mathrm{d}\vec{\xi}. \tag{1.1}$$

The statistical moments such as the mean and standard deviation can then be calculated. The SC method solves this problem by approximating the functional relationship between the outputs of interest $X(\vec{\xi})$ and the random inputs $\vec{\xi}$ using an expansion in Lagrange polynomials. This results in

the one-dimensional case with one uncertain input parameter $\xi$,

$$X(\xi)^i \approx \sum_{j=1}^{N} X(\xi_j)^i L_j(\xi), \tag{1.2}$$

with $L_j(\xi)$ the Lagrange polynomials defined as

$$L_j(\xi) = \prod_{\substack{k=1 \\ k \neq j}}^{N} \frac{\xi - \xi_k}{\xi_j - \xi_k}, \tag{1.3}$$

such that $L_j(\xi_k) = \delta_{jk}$ with $\delta_{jk}$ the Kronecker delta. The coefficients $X(\xi_j)$ are solutions of the aeroacoustic problem for the realization $\xi_j$ for the random input parameter $\xi$.

The deterministic sampling points $\xi_j$ in the SC method are usually chosen to be numerical quadrature points, because they are accurate for computing the integrals (Eq. (1.1)). Standard Gauss-quadrature requires recomputing each modal coefficient in Eq. (1.2) each time $N$ is increased, which is prohibitive for LES. In the present study, we use the Clenshaw–Curtis[35] (CC) quadrature points for the sampling points $\xi_j$ given by $\xi \in [-1, 1]$

$$\xi_j = -\cos\left(\frac{\pi(j-1)}{N-1}\right). \tag{1.4}$$

The points are linearly scaled for input parameters on other ranges. These points are nested in the sense that all points $\xi_j$ are re-used when increasing the quadrature level $l$, allowing to keep the abscissae when $N$ is increased, with $N = 2^l + 1$ for $l > 0$ and $N(0) = 1$. Substituting Eq. (1.2) into Eq. (1.1) leads to the approximation

$$\mu_{X_i} \approx \sum_{j=1}^{N} X(\xi_j)^i w_j, \tag{1.5}$$

with integration weights $w_j$

$$w_j = \int_{\Xi} L_j(\xi) f_\xi(\xi) \mathrm{d}\xi. \tag{1.6}$$

The SC method can be extended to multiple independent input uncertainties using the following isotropic full tensor product extension into $n_\xi$ dimensions $\vec{\xi} = \{\xi_1, \ldots, \xi_{n_\xi}\}$

$$\mu_{X_i} = \sum_{j_1=1}^{N} \cdots \sum_{j_{n_\xi}=1}^{N} X(\xi_{j_1}, \ldots, \xi_{j_{n_\xi}})^i w_{j_1} \cdots w_{j_{n_\xi}}. \tag{1.7}$$

The stochastic input $\vec{\xi}$ or output $X(\vec{\xi})$ can also depend on other parameters such as spatial coordinates (velocity profiles and maps, pressure coefficient) or frequency (wall-pressure and far-field acoustic pressure power spectral density (PSD)). The final value of the stochastic expansion of the analyzed variable (maximum value of $N$) is termed $P$.

## 4. Sound Prediction Methods

As shown by Roger & Moreau,[26] the trailing-edge noise can be obtained by iteratively solving scattering problems at the airfoil edges. The main trailing-edge scattering obtained by Amiet[36] has been corrected by a leading-edge back-scattering contribution that fully accounts for the finite chord length. The random predicted sound field at a given observer location $\mathbf{x} = (x_1, x_2, x_3)$ and for a given radian frequency $\omega_f$ (or wavenumber $k_f$) then reads

$$S_{pp}(\mathbf{x}, \omega_f) = \left(\frac{\omega_f C x_3}{2\pi c_0 S_0^2}\right)^2 \frac{L}{2} |\mathcal{L}|^2 \Phi_{pp}(\omega_f) l_y(\omega_f), \tag{1.8}$$

where $\Phi_{pp}$ is the wall-pressure power spectral density and $l_y$ the spanwise correlation length near the trailing edge assumed to be deterministic. The radiation integral $\mathcal{L}$ of which parameters are both the free stream velocity $U_\infty$ and the convection speed can be found in Roger & Moreau.[26]

In case of rotation, the far-field noise PSD of a low solidity fan with $B$ independent blades is given by an integration over all possible azimuthal positions[22] of the single airfoil formulation (1.8)

$$S_{pp}(\mathbf{X}, \omega_f) = \frac{B}{2\pi} \int_0^{2\pi} \left(\frac{\omega_e(\Psi)}{\omega_f}\right)^2 S_{pp}^{\Psi}(\mathbf{x}, \omega_e) d\Psi. \tag{1.9}$$

The factor $\omega_e(\Psi)/\omega_f$ accounts for Doppler effects caused by the rotation ($\omega_e$ emission angular frequency). The fan noise predictions therefore rely on a strip theory combined with an acoustic analogy,[37] originally developed by Schlinker & Amiet[22] for helicopter rotor's trailing-edge noise, and extended to finite chord lengths and general three-dimensional gusts by Roger & Moreau,[26] and applied to low speed fans by Moreau & Roger.[38] Recently Sinayoko *et al.* has shown that this approximation of locally translating airfoils is accurate except at transonic speeds.[39] In order to take into account the variation of the flow along the blade span, the latter is split into 5 equal segments from hub to tip as in Christophe *et al.*,[25] and the total radiated sound is then the summation of the sound emitted by each airfoil strip.

When an unsteady LES computation is used, the wall-pressure spectra $\Phi_{pp}$ at the trailing edge is directly extracted from the simulations. In the RANS simulations, all variables are time-averaged and the wall-pressure fluctuations are reconstructed from the mean flow. Two such models are considered.

The YR model only uses integral boundary-layer parameters and reads

$$\frac{\Phi_{pp}(\omega_f)\,U_e}{\tau_w^2\,\delta} = \frac{0.78\,(1.8\,\Pi\,\beta_C + 6)\,\left(\frac{\omega_f\,\delta}{U_e}\right)^2}{\left[\left(\frac{\omega_f\,\delta}{U_e}\right)^{0.75} + 0.5\right]^{3.7} + \left[1.1\left(\frac{\omega_f\,\delta}{U_e}\right)\right]^7}, \tag{1.10}$$

where Clauser's parameter is $\beta_C = (\Theta/\tau_w)(dp/dx)$ and Coles' parameter $\Pi$ is given by the implicit law of the wake:[40] $2\,\Pi - \ln(1+\Pi) = \frac{\kappa\,U_e}{u_\tau} - \ln\left(\frac{\delta^*\,U_e}{\nu}\right) - \kappa\,C - \ln\kappa$ ($\Theta$ the momentum thickness, $\kappa$ the von Kármán constant and $C$ a constant in the log law). For Eq. (1.10), the original expression[41] based on $\delta$ has been preferred to the formulation recently proposed by Rozenberg *et al.*[17] based on $\delta^*$, as it provides a better agreement with the experimental data for the CD airfoil.[8,23,42] As explained by Rozenberg *et al.*,[17] the friction velocity $u_\tau$ is obtained from extended Clauser plots rather than direct upwind finite-difference estimates. Similarly the wake law is also verified graphically by comparing the model with the measured dimensionless velocity log plots ($u^+$, $y^+$).

Using the PL model,[24] Remmler *et al.*[18] derived an expression for the wall-pressure spectrum

$$\Phi_{pp}(\omega_f) = 8\rho^2 \iiint_0^\infty \frac{k_f^1(\omega_f)^2}{k_f(\omega_f)^2} \exp^{-k_f(\omega_f)(y+\hat{y})} ... \\ S_{22}(y,\hat{y},\omega_f)\frac{\partial U_1}{\partial y}\frac{\partial U_1}{\partial \hat{y}} dy d\hat{y} dk_f^3 \tag{1.11}$$

with the energy spectrum of the vertical velocity fluctuations:

$$S_{22}(y,\hat{y},\omega_f) = \frac{\overline{u_2'}(y)\overline{u_2'}(\hat{y})}{\pi^2}\Lambda^2 \iint_0^\infty R_{22} ... \\ \cos(\alpha\,k_f^1(\omega_f) r_1)\cos(\alpha k_f^3 r_3) dr_1 dr_3. \tag{1.12}$$

The model therefore uses the wall parallel velocity profile $U_1$ and the wall perpendicular velocity fluctuation profile $u_2'$. Following the procedure outlined by Remmler *et al.*,[18] both velocities and the velocity correlation length scale $\Lambda$ are calculated from the RANS outputs and the velocity correlation

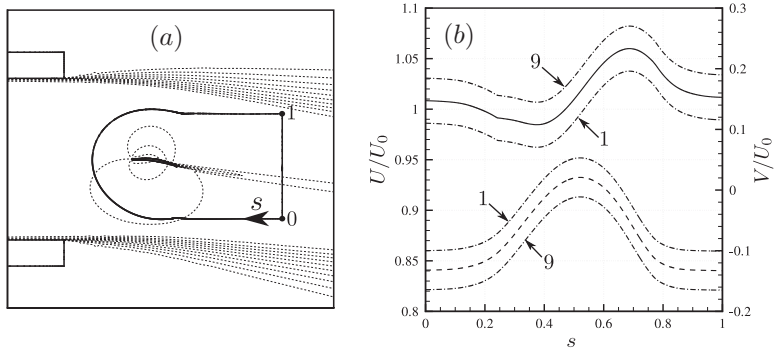


Fig. 1.2. (a) Parameterization of inlet boundary condition (solid line) and velocity magnitude contours (dash line), levels 0–1.7 with increment 0.1. (b) Parametric inlet velocity profiles: (plain) streamwise velocity $U$, (dash) crosswise velocity $V$ and (dash-dot) uncertainty bounds around inlet profiles.

function $R_{22}$ and the scale anisotropy factor $\alpha$ are modelled. No quadratures are used to calculate the quintuple integral in Eq. (1.11) as they would require prohibitive memory. The integration is performed with a Monte Carlo method using importance sampling for enhancing convergence. More details on this model can be found in Remmler *et al.*[18]

## 5. Controlled-Diffusion Airfoil

### 5.1. *Deterministic flow simulations*

The present computations consider the Controlled-Diffusion (CD) airfoil studied previously.[4–9] This profile corresponds to the mid-span section of a typical automotive cooling fan with 9 symmetric blades, the H380EC1 fan blade considered in Sec 6.[43] It has a 4% relative thickness and a leading-edge camber angle of 12°. The airfoil chord length is $C = 0.1356$ m. It is set at a geometrical angle of attack of $\alpha_w = 8°$. The reference velocity is $U_0 = 16$ m/s, yielding a Reynolds number based on the airfoil chord length $\mathrm{Re}_C$=1.6×10$^5$. Further details on the experimental setup and flow conditions can be found in Moreau *et al.*[23]

The RANS computations are obtained with the Ansys Fluent 12 solver using the Shear-Stress-Transport (SST) $k-\omega$ turbulence model.[44] Unlike several $k-\epsilon$ models, the SST model was shown to properly capture the laminar recirculation bubble on this airfoil.[23] Second-order schemes are used for spatial discretization of all variables. The RANS computations

use a no-slip boundary condition on the airfoil surface, a convective outflow boundary condition at the exit plane, and velocities ($U$ and $V$) from the wind tunnel computation at the inlet. RANS simulations were run until a convergence to machine accuracy was reached.

The LES are based on the spatially filtered, incompressible Navier-Stokes equations with the dynamic subgrid-scale model.[45,46] These equations are solved using energy-conserving non-dissipative central difference schemes for spatial discretization and the fractional-step method for time advancement,[47] leading to the control-volume solver CDP originally developed by Mahesh *et al.*,[48] for hybrid unstructured grids. Details on the numerical schemes for the current unstructured solver can be found in Ham & Iaccarino.[49] The mesh taken from Moreau *et al.*[5] and labelled *CDP-B* is similar to the structured mesh of Wang *et al.*[8] but a spanwise grid coarsening proportional to the distance from the airfoil is performed to reduce the overall number of nodes to 1.5 million. The spanwise extent of the computational domain is again taken to be 10% of the chord length, which is enough to capture the experimental correlation length for this flow condition.[8,42] *CDP-B* LES results were shown to compare very well with both experimental wall-pressure and wake-velocity data.[5] Except in the vicinity of the leading edge, the near-wall grid resolution on the suction side is $\Delta x^+ \leq 34$, $\Delta y^+ \leq 1$, and $\Delta z^+ \leq 20$ in wall units, which is adequate for LES.[50] On the pressure side, the resolution is coarser because the boundary layer is laminar. The same inflow/outflow conditions as for the RANS are used. Periodic boundary conditions are applied in the spanwise direction. For the LES simulations that were run, a dimensionless time step of $2.5 \cdot 10^{-4}$, normalized by the chord $C$ and the reference velocity $U_0$, is used leading to a CFL smaller than one in the whole domain. After a steady state was reached, airfoil trailing-edge surface pressure and flow statistics were collected for 50 flow-through times to simultaneously yield a sufficiently high spectral resolution (10 kHz) and a good statistical convergence of the low frequency spectral components (down to 100 Hz).

### 5.2. *Characterization of the random variables* $\vec{\xi}$

Figure 1.2(a) shows iso-contours of velocity magnitude from a RANS computation on the full wind tunnel configuration (LWT). The wind tunnel velocity was set to the nominal value $U_t/U_0 = 1$. On the same figure, the boundary of the restricted computational domain is represented, showing that the restricted domain is fully embedded in the inviscid jet potential

core between the nozzle shear layers. The velocity components ($U$ and $V$) from this simulation are interpolated on the boundaries of the restricted domain and are used as inlet conditions of the following steps for the methodology described in Sec. 2. The averaging along the curvilinear abscissa $s$ of the inlet velocity profiles shown in Fig. 1.2 (b) provides an inlet velocity vector as shown in the sketch in Fig. 1.3. A corresponding inlet flow angle relative to the airfoil chord $\alpha_e$ (see definition in Fig. 1.3) can be computed and is found as 4° for the reference numerical deterministic case having a geometrical angle of attack of 8°. The physical variations observed in the experimental flow measurements are taken into account by selecting a 2.5% uncertainty bound on the streamwise velocity $U$ and a 10% uncertainty bound on the crosswise velocity $V$ that include the short-scale fluctuations seen in the experimental profiles. Further details on the selection of the uncertainty bounds can be found in Christophe *et al.*[6] These conservative uncertainty ranges for both velocity components are also consistent with the observed variations found in the RANS simulations with different turbulence models.[23] The corresponding bounds of inlet flow angle $\alpha_e$ are $[6°, 2°]$, and the relative angular variation $\Delta\alpha_e$ with respect to the above reference case ($\alpha_e = 4°$) or simulation #5 is then $[2°, -2°]$ (see Table 1.1). The same computational mesh is used for all computations as only the inlet flow angle $\alpha_e$ is varied through the boundary conditions while the geometrical angle of attack $\alpha_w$ is kept constant. Furthermore, due to the small variations of the inlet flow angle, the airfoil wake angle remains close to the reference case for all computations and therefore the same grid extent can be used for all computations without having any interaction with the domain boundary conditions. The upper and lower bounds of the velocity profiles are shown in Fig. 1.2, together with the deterministic profiles. Both components $U$ and $V$, and consequently the inlet flow angle $\alpha_e$, are assumed to be random variables ($\vec{\xi}(\gamma) \equiv (U(\gamma), V(\gamma))$ or $\xi(\gamma) \equiv \alpha_e(\gamma)$) with uniform distribution $\zeta$ of the random perturbation parameter $\gamma$ within their interval of variation. From those bounds, a set of 17 velocity inlet profiles ($P$=17 in Eq. (1.2)) are determined using a Clenshaw-Curtis quadrature.[35] A total of 17 corresponding RANS computations are run showing a sufficient convergence of the stochastic collocation method for 9 samples, as explained in Sec. 5.3.2, and only 9 LES computations are then run ($P$=9 in Eq. (1.2)). Table 1.1 summarizes the inlet flow angle variation for the 9 samples with $\gamma$. MC simulations of the RANS case have also been achieved to check the accuracy of the SC and demonstrate its efficiency. In the selected interval about a thousand samples are needed to statistically converge (maximum number

Table 1.1. Variation of the geometrical angle of attack $\alpha_w$ and the inlet flow angle $\alpha_e$ with the random perturbation parameter for 9 samples.

| Sample | #1 | #2 | #3 | #4 | #5 | #6 | #7 | #8 | #9 |
|---|---|---|---|---|---|---|---|---|---|
| $\gamma$ | $-1$ | $-0.93$ | $-0.71$ | $-0.38$ | 0 | 0.38 | 0.71 | 0.93 | 1 |
| $\alpha_w$ | 8 | 8 | 8 | 8 | 8 | 8 | 8 | 8 | 8 |
| $\alpha_e$ | 6 | 5.86 | 5.42 | 4.76 | 4 | 3.24 | 2.58 | 2.14 | 2 |
| $\Delta\alpha_e$ | 2 | 1.86 | 1.42 | 0.76 | 0 | $-0.76$ | $-1.42$ | $-1.86$ | $-2$ |

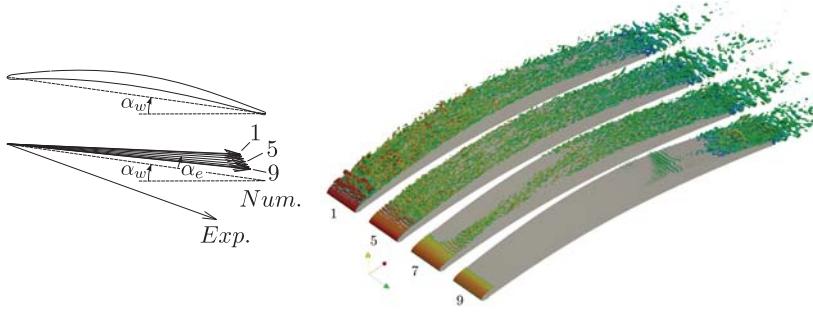


Fig. 1.3. Isosurfaces of the {$Q$ factor ($QC^2/U_0^2 = 2000$) coloured by velocity magnitude for inflow conditions corresponding to LES computations # 1,5,7,9.

of samples $P = 1000$), which makes the stochastic collocation based on Clenshaw-Curtis quadrature method about two orders of magnitude faster for the present study, as it will be illustrated later.

## 5.3. *UQ results*

### 5.3.1. *Flow topology*

Changes in flow kinematics with the inlet flow angles $\alpha_e$ are described by iso-surfaces of $Q$ factor in Fig. 1.3. This second invariant of the velocity-gradient tensor helps define vortices and visualize the turbulence development. In LES #1 and #5 (reference), the flow around the airfoil is found similar as in previous studies.[5,6] Small instabilities form close to the reattachment point of the laminar recirculation bubble that trigger transition. The flow tends to re-laminarize toward mid-chord due to the favourable pressure gradient (less turbulent structures and thinner boundary layer). When this gradient becomes adverse at mid-chord, the turbulent boundary layer thickens again and larger turbulent structures appear near the trailing edge. With the increase of the inlet flow angle, more intense structures are

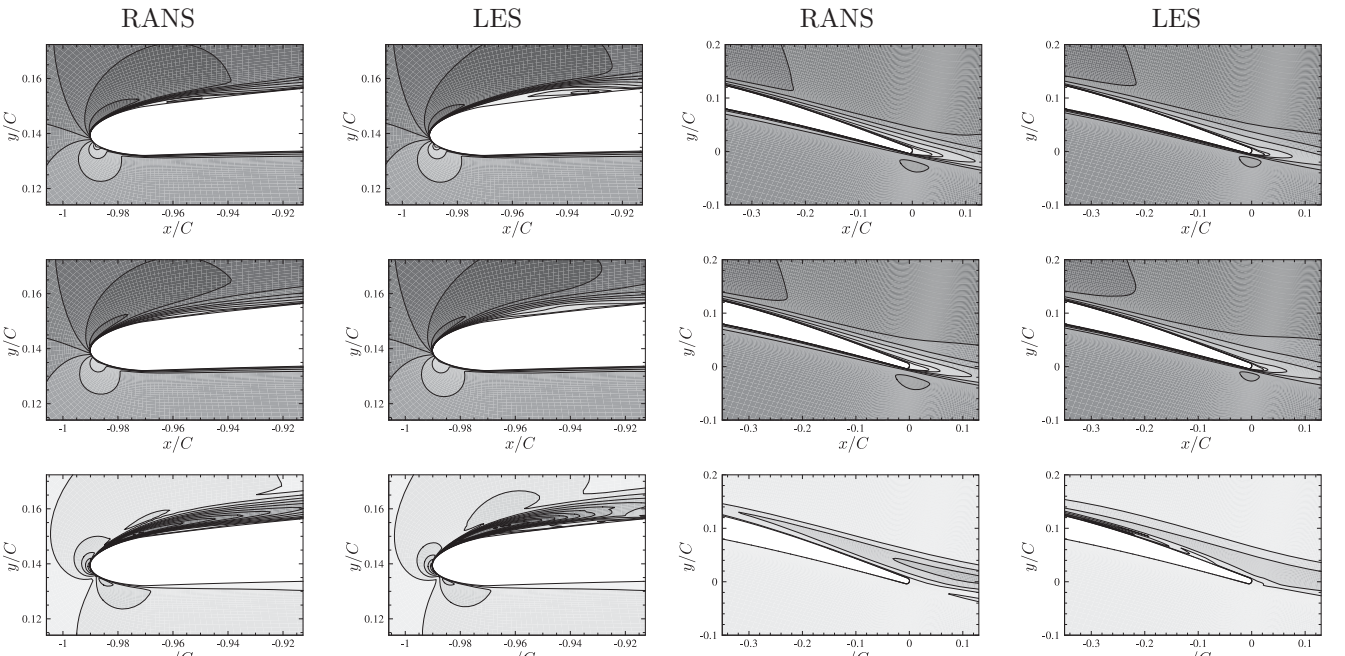


Fig. 1.4. Iso-contours of velocity magnitude around the leading edge and trailing edge. (Top) Deterministic computation # 5, (middle) mean and (bottom) standard deviation of all computations. Contour levels for mean values (0,0.1:0.2:2) and standard deviation (0:0.05:0.75).

formed after the recirculation region at the leading edge; those structures being then convected along the blade chord. In LES #7, the acceleration around the leading edge still yields a weak flow separation at the leading edge, which is not strong enough to trigger transition over the whole span (the Kelvin-Helmholtz instability and roll up has disappeared). Turbulence only develops over a narrow strip and only the adverse pressure gradient after mid-chord triggers transition and the turbulence development over the whole span. In LES #9, the acceleration around the leading edge is no longer strong enough to trigger a flow separation at the leading edge and no transition occurs before mid-chord. Flow separation occurs beyond mid-chord that triggers the transition close to the trailing edge. Instabilities are observed in the recirculation region beyond mid-chord but do not cause any transition in the boundary layer due to their low intensity. Finally, weak vortex shedding is seen in the near-wake on the pressure side for all cases.

Figure 1.4 shows iso-contours of velocity magnitude for the computation #5 (deterministic reference computation) and for the mean and standard deviation from the 9 samples used in the SC method for both RANS and LES computations. These maps are obtained by applying Eq. (1.2) for the time-averaged velocity at each grid point from all the different deterministic computations. Only views around leading and trailing edges are shown since main variations of the flow occur in those regions. For both regions, the flow is found globally similar between the deterministic solution and the mean solution for both RANS and LES computations, and similar between the LES and RANS computations. In the leading-edge region, a larger and thicker recirculation zone is observed in the LES computations, for the deterministic computations #5 and the mean solution. A larger localized production of standard deviation is present in the recirculation region of the RANS computations, caused by a larger variation of the recirculation zone with the inlet flow angle compared with the LES computations. This observation is consistent with the variation of the length and position of the leading-edge recirculation bubble that can be determined from the wall-friction coefficient, as reported in Christophe *et al.*[6] The RANS computations show a monotonic decrease of the size of the recirculation bubble at the leading edge with the decrease of the inlet flow angle from computation #1 to #7, while no systematic decrease of the size of the recirculation bubble is observed in LES computations. In the trailing-edge region, the main difference is appearing beyond mid-chord and before the trailing edge, where a region of higher standard deviation is observed in the LES computations and is not present in the corresponding RANS computations. This

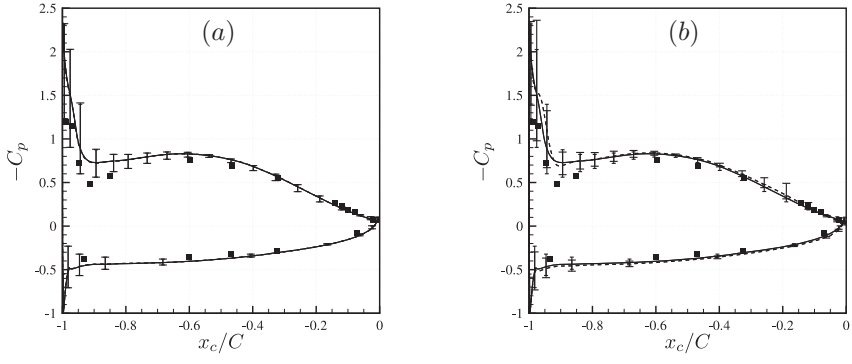


Fig. 1.5. Mean wall-pressure coefficient $-C_p$ ($U_0$ = 16 m/s, $\mathrm{Re}_C$=1.6×10$^5$). Experiment[42] (square). (a) Comparison of RANS UQ based methods: SC (plain line and small uncertainty bars) and MC (dashed line and large uncertainty bars). (b) Comparison of flow prediction method using SC: RANS computations (plain line and small uncertainty bars) and LES computations (dashed line and large uncertainty bars).

is caused by the presence of a secondary recirculation zone appearing in the LES computations #8 and #9, and not observed in RANS computations. It should be stressed that this transition in the LES occurs suddenly for a very small variation of incidence in the last two runs (LES #8 and #9).

The differences observed between the RANS and LES computations highlight the complexity of the present problem and the influence of the physical model on the flow topology. The present RANS computations involve fully turbulent flows and therefore cannot correctly take into account laminar and transition regions whereas LES calculations with the present dynamic SGS model do, at least for the location and the early stage of transition.[51]

### 5.3.2. *Wall-pressure coefficient*

The UQ results on the wall-pressure coefficient $-C_p$ are shown in Fig. 1.5 and compared with experimental results[42] in terms of the mean coefficient (lines) and the intervals, which represent the propagation of 100% of the considered input uncertainty. They are obtained by applying Eq. (1.2) to the wall-pressure distribution. The minimum and maximum of the uncertainty bars are obtained from the minimum and maximum of the response surface from Eq. (1.2). Since the airfoil has a geometrical angle of attack, the chordwise coordinate $x_c = x/\cos\alpha_w$ is used to represent data along the blade chord. Using this coordinate system, the leading edge is located at

$x_c/C = -1$ and the trailing edge is at $x_c/C = 0$. In Fig. 1.5(a), the two stochastic methods are compared using the RANS data set. Both MC and SC methods agree very well yielding the same mean solution and almost identical uncertainty bars. They both show larger uncertainty bars in the leading-edge region and particularly on the suction side in the recirculation bubble. Even though the uncertainty bars are smaller at the trailing edge because of the low value of the mean $C_p$, the local coefficient of variation is significant. In Fig. 1.5(b), the SC for both RANS and LES are compared. Again, for both RANS and LES computations, larger uncertainty bars are observed in the leading-edge region. Main differences are appearing in the aft region where the second laminar recirculation bubble occurs for the lowest incidences in the LES computations, and not observed in the corresponding RANS computations. If the last two LES results (#8 and #9) were to be removed, the LES would clearly be comparable to the RANS calculations. This shows the complexity of the problem and the large range of flow topologies appearing in the present LES that cannot be captured by the RANS computations due to the simpler RANS model used, as described in the previous section. In regions where the mean simulation result shows a larger difference with respect to the experimental data, the uncertainty bars are also relatively large and account to a large extent for this difference. Both RANS and LES stochastic data sets compare quite well with experiments. The convergence of both stochastic methods for the RANS computations was assessed on this $-C_p$ profiles in Christophe *et al.*[6] The convergence rate of the MC method is found to be $\mathcal{O}(N^{-1})$ while the SC method is found to be $\mathcal{O}(N^{-4})$, which stresses the efficiency of the SC method for a limited number of uncertain variables (curse of dimensionality). Lower convergence rate of the SC method using LES computations is observed because of the large range of flow topologies found in these computations. Similar UQ results for the streamwise boundary-layer velocity profiles, in terms of uncertainty bars and convergence, at the last remote microphone probe (RMP #25, $x_c/C = -0.02$) where the sources of trailing-edge noise are mainly concentrated, can also be found in Christophe *et al.*[6] From these boundary-layer velocity profiles, the necessary boundary-layer parameters for the consequent models of the wall-pressure spectra can be inferred.

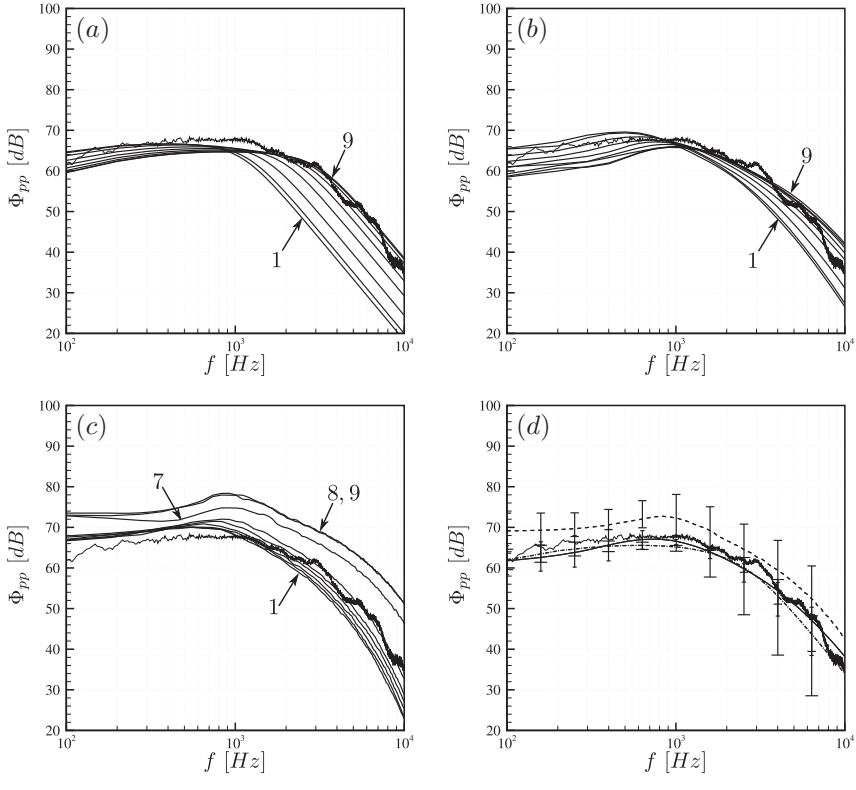


Fig. 1.6. Wall pressure frequency spectra ($p_{ref}$ = 20 mPa) in the trailing-edge area ($x_c/C = -0.02$, RMP # 25) using (a) YR and (b) using PL model for all RANS computations. (c) LES wall-pressure spectra. (d) Comparison of wall-pressure spectra based on RANS and LES inputs in terms of mean and uncertainty bars, YR model (dash-dot and large uncertainty bars), PL model (plain and small uncertainty bars), LES (dash and medium uncertainty bar). Experiment (thin plain).

### 5.3.3. *Wall-pressure statistics near the trailing edge*

The corresponding trailing-edge spectra of the two methods described above are shown respectively in Figs. 1.6(a) and 1.6(b) for the 9 samples used for SC. A similar behaviour is found for both models where the higher spectrum amplitude at low frequencies corresponds to computation #1 (high inlet flow angle) and the lower one corresponds to computation #9 (lower inlet flow angle). At high frequencies, a reverse behaviour of the models is observed. For both models, a monotonic variation of the wall-pressure spectrum appears going from computation #1 to #9. For both models, a similar

crossing is identified around 1 kHz. The YR model presents large variations of the various spectra at high frequencies due to the large uncertainties involved in the wall shear-stress determination, from which the model derives information about the high frequency content. The PL model, not based on the wall shear-stress variable, shows less variations of the wall-pressure spectrum at high frequencies. Yet, at low frequencies, they are larger mainly caused by the slow statistical convergence of the Monte-Carlo integration technique used to integrate the boundary-layer profiles in Eq. (1.11). The corresponding LES spectra for the 9 samples are shown in Fig. 1.6(c) and two groups of LES results are obtained. On the one hand, the LES #1 to #6 are similar as the reference calculation (LES #5) and show similar variations as the RANS reconstructed spectra. On the other hand, the LES #7 to #9 show larger pressure fluctuations for all frequencies due the recirculation bubble close to the trailing edge triggering a more intense turbulent boundary layer than in other cases.

The wall-pressure PSD $\Phi_{pp}$ is now used as the stochastic variable in Eq. (1.2). Figure 1.6(d) shows the comparison of all methods with the measured one at RMP #25, in terms of mean and the confidence interval, which represents the propagation of 100% of the considered input uncertainty. Good agreement with experiments is found on the mean wall-pressure spectrum for both methods using RANS information. Larger uncertainty bars are found at high frequencies using the YR model and at low frequencies using the PL model, following explanations given previously. The higher spectra obtained in LES #7 to #9 cause the mean pressure spectrum of the LES to be shifted to higher levels by about 8 dB. Consequently, the LES uncertainty bars are also found to be larger than those of the RANS computations and could be more comparable if the last two simulations were discarded.

### 5.4. *Stochastic acoustic predictions*

The corresponding sound results are reported in Fig. 1.7, together with the experimental measurements (their uncertainty is $\pm 1$ dB). The far-field acoustic-pressure PSD $S_{pp}$ is the stochastic variable of interest in Eq. (1.2). Mean sound predictions obtained from RANS reconstructed spectra compare favourably with the experimental far-field sound. Similar uncertainty differences between the two RANS-based models YR and PL are observed due to the direct propagation of the uncertainties seen in the trailing-edge wall spectra. Larger uncertainty bars are found at high frequencies using

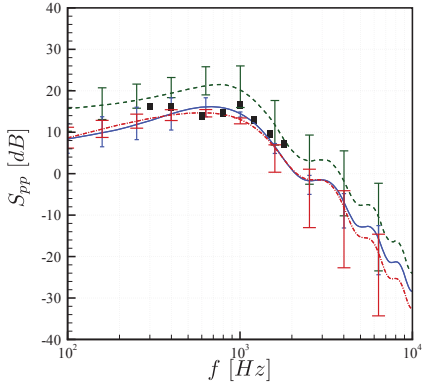


Fig. 1.7. Means and uncertainty bars of far field acoustic spectra ($p_{ref}$=20 mPa) for the different prediction methods, in the mid span plane above the airfoil ($\theta = 90°$) at $R = 2$ m from the trailing edge. YR model (Dash-dot and large uncertainty bars — red), PL model (plain and small uncertainty bars — blue), LES (dash and medium uncertainty bar — green). Experiment (Square).

the YR model and at low frequencies using the PL models. Again, the LES presents an overestimate compared with the experiments caused by the over-prediction of the wall-pressure spectrum. The corresponding uncertainty bars are then also propagated through the acoustic method.

## 6. Low-Speed Axial Cooling Fan

### 6.1. *Deterministic flow simulations*

As mentioned above the low-speed fan considered here is the H380EC1 designed for a best efficiency point at a volume flow-rate $\dot{Q}$ of 2500 m$^3$/h at a rotational speed $\Omega$ of 2500 rpm.[15,38,43,52] The rotor is flush mounted on a plenum walls from which the static pressure rise across the fan $\Delta p$ is measured. The available experimental data mostly include overall performances and acoustic power measurements at several flow-rates and rotational speeds obtained in a reverberant wind tunnel. The plenum is assumed axisymmetric so that a single blade passage, including the actual tip gap, is modeled and matching nodes are used at the periodic boundary conditions.[52] The flow is modelled with RANS computations using the Shear-Stress-Transport (SST) $k-\omega$ turbulence model in the ANSYS CFX 14 solver. The mesh has a total of 5.1 million hexahedral elements, and is refined in the boundary-layers around the blade to reach dimensionless

distances to the wall $y^+$ less than 5 in the trailing-edge region, where presently most of the sound production occurs. The volume flow-rate is set on the inlet surface of the plenum. The average pressure on the outlet surface is set to the reference pressure. Low-dissipation second-order numerical schemes are used for the flow variables (velocity and pressure), and a first-order scheme for the transport of turbulent quantities. To yield repeatable and consistent results, once the maximum convergence is reached, solutions are averaged over the last 500 iterations.

## 6.2. *Characterization of the random variables* $\vec{\xi}$

As introduced above, only the parameters defining the operating conditions are considered for uncertainty quantification in a first step. The volume flow rate is defined with a 5% error bound around 2500 $m^3/h$. The variation of this variable mainly depends on discrete events, such as dirt in the upstream heat exchanger, quality and nature of the fan, and cooling module assembly and manufacturing. A uniform probability density function (PDF) is therefore considered. The variation of rotational speed mainly depends on the motor manufacturing quality and is thus defined by a Gaussian PDF as fit on the manufacturing lines. A usual process dispersion for automotive electrical motors is $\pm 100$ rpm. The rotational speed is thus defined with a 4% error bound around 2500 rpm. For those two variables considered independently, a set of nine RANS computations are determined using a Clenshaw-Curtis quadrature that provides similar convergence as the midspan CD airfoil described in Sec. 5.3.2. For the two-dimensional uncertainty quantification involving both variables, a full tensor grid of 81 RANS computations is used.

## 6.3. *UQ results*

### 6.3.1. *Wall-pressure distribution and fan performance*

One dimensional (1D) results on the operating conditions are first analyzed in Fig. 1.8 showing the iso-contours of the standard deviation from the 9 samples used in the SC method for each variable (volume flow rate and rotational speed), on the suction and pressure sides of the blade. The two considered parameters are influencing different zones of the blade surface. For the volume flow rate, a large standard deviation is observed on the suction side of the airfoil, especially at the tip of the blade near the trailing-edge region, due to large variations of the recirculation zone under the

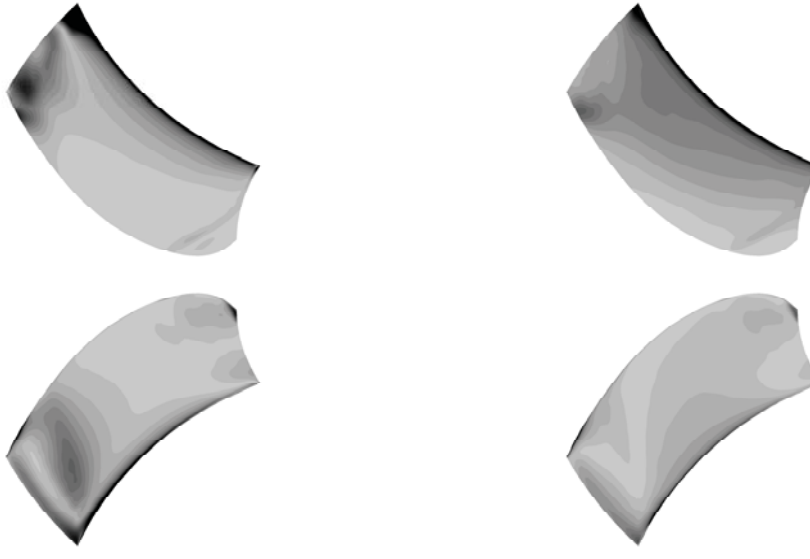

Fig. 1.8. Iso-contours of the standard deviation of the static pressure on (top) suction side (contour levels [0:2:40]) and (bottom) pressure side (contour levels [0:1:20]). (Left) Variation of the volume flow rate and (right) variation of the rotational speed.

rotating ring, as it has been already highlighted in the URANS and SAS simulations on this fan.[52] A second zone of large standard deviation is also observed at the hub on the pressure side corresponding to the flow detachment at the blade leading edge created by the blade cusp. In case of rotational speed variations, the standard deviation of the pressure presents large amplitudes on a broader part of the blade, on both sides, around the leading edge up to mid-chord. The volume flow rate thus mainly influences the size of the recirculation zones while the rotational speed modifies the complete blade pressure distribution.

A comparison of the fan overall performances with the error bar emphasizing the uncertainty interval in case of $\dot{Q}$ variations is presented in Fig. 1.9 for the pressure rise. Two experimental curves are provided as they represent the maximum experimental range of variations obtained on this fan between the many mock-ups and prototypes tested. It should be stressed that the error range on the volume flow rate was chosen to cover the experimental uncertainty, and the resulting uncertainty range on the pressure rise matches the experimental scattering well.

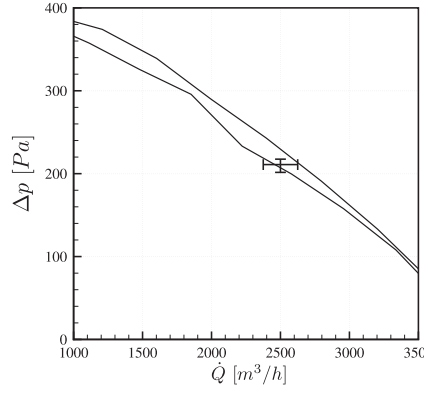


Fig. 1.9. Fan performance.

### 6.4. *Stochastic acoustic predictions*

In Figs. 1.10–1.12, the spectra of the total simulated sound PoWer Level (PWL) for both YR and PL models are compared with two sets of experimental data, one collected on an engine cooling module in a semi-anechoic chamber[38] and one collected in a reverberant wind tunnel.[53] Both models yield good agreement with the experimental broadband spectra stressing the significant contribution of this noise mechanism at design condition. The PL model presents a small under-prediction of about 3 dB over the whole frequency range, but a better overall shape especially at low frequencies compared with the reverberant wind tunnel data.

Figure 1.10 provides the 1D UQ results for a variation of $\dot{Q}$ for the YR and PL models respectively. The simulated PWL corresponding to the different strips discretizing the blade are shown together with their uncertainty bars. As shown in Moreau *et al.*,[52] the obtained sound spectra have similar shapes, amplitudes and uncertainties than the trailing-edge wall-pressure spectra, showing a direct propagation of the amplitudes and uncertainties through the noise propagation model. Larger uncertainties are obtained in the hub and tip regions as observed previously. The largest uncertainty bars at low frequencies in the tip region correspond to the large standard deviations seen in Fig. 1.8 and are related to the local large-scale flow separation under the fan ring. In the PL model, some lack of convergence in the integration of Eq. (1.11) by a Monte Carlo method could also contribute. At the hub, the largest uncertainties could be traced to the small scale structures created by the blade cusp. The total sound radiated

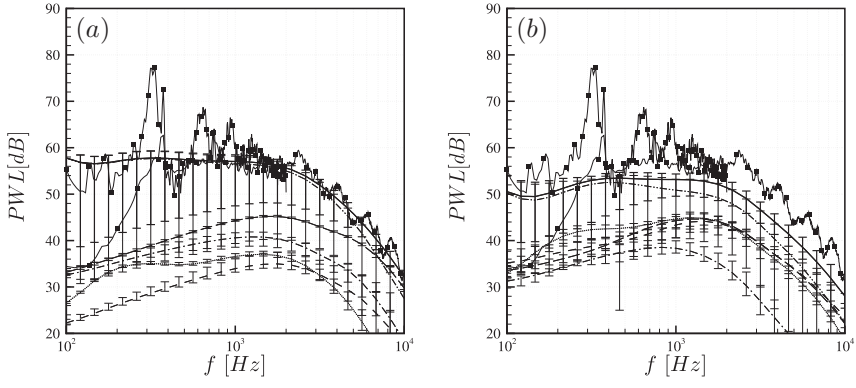


Fig. 1.10. 1D UQ on $\dot{Q}$: (a) YR model and (b) PL model. Total sound (solid bold), strip 1 (dash), strip 2 (dash-dot), strip 3 (dot), strip 4 (long dash), strip 5 (dash-dot-dot), experiment[38,53] (symbols). $p_{ref} = 20$ mPa.

by the complete blade is mainly caused by the noise emitted by the tip strip #5 with almost similar mean amplitudes. At high frequencies, strip #4 also contributes to the total sound spectrum for the YR model while almost all blade strips contribute for the PL model. Moreover, the uncertainty bars for the complete blade are reduced compared with those of the tip strip. The complete fan noise spectrum is thus dominated in amplitude by the tip region while the uncertainty bars are related to uncertainties observed along the complete blade span. A proper control of the flow along the complete blade span is then necessary to reduce the uncertainties on the radiated sound. Finally, the PL model seems to yield lower overall uncertainty than the YR model.

Figure 1.11 shows the corresponding 1D UQ results for a variation of $\Omega$ for both YR and PL models. The same mean total spectrum dominated by the tip strip is obtained. The uncertainties (less than 1 dB) are however much smaller than for a variation of flow rate. Therefore the process dispersion on the rotational speed does not trigger significant uncertainties on the fan trailing-edge noise.

Figure 1.12 shows the corresponding 2D UQ results for variations of both $\dot{Q}$ and $\Omega$ for the YR and PL models respectively. A similar mean total spectrum dominated by the tip strip is again obtained. The uncertainty bars for both models now lie in between both 1D UQ results on each separate performance parameter, yielding 2 to 6 dB for the YR model and 3 to 4 dB. The PL model therefore gives smaller uncertainties than the YR

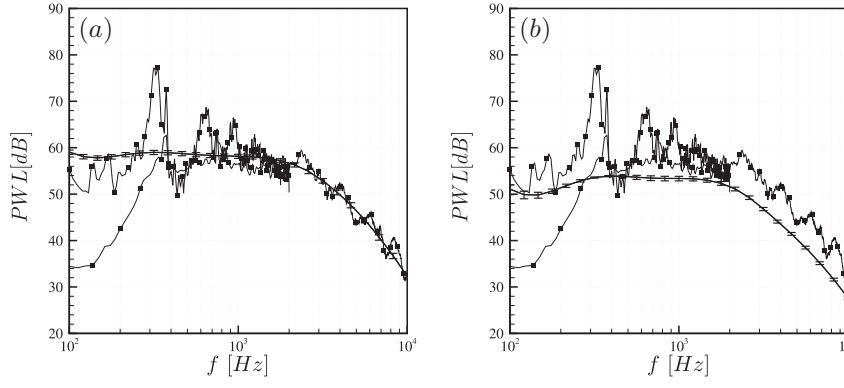


Fig. 1.11. 1D UQ on Ω: (a) YR model and (b) PL model. Total sound (solid bold) and experiment[38,53] (symbols). $p_{ref} = 20$ mPa.

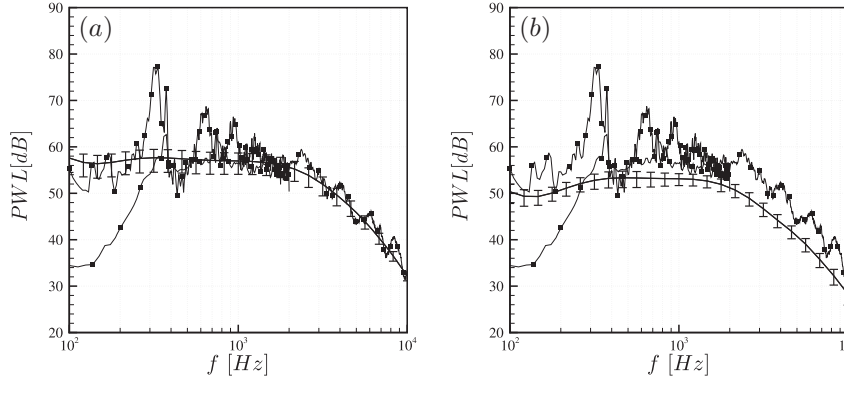


Fig. 1.12. 2D UQ: (a) YR model and (b) PL model. Total sound (solid bold) and experiment (symbols). $p_{ref} = 20$ mPa.

model, more uniformly spread over the whole frequency range.

## 7. Conclusions

The uncertainty quantification (UQ) related to the self-noise prediction based on a RANS flow computation of a low-subsonic axial fan has been achieved. As the methodology used for fan noise prediction is based on airfoil theories, the uncertainty quantification of a low-speed Controlled-Diffusion (CD) airfoil has been first considered. In both applications, the

noise predictions are obtained using Amiet's theory requiring the wall-pressure spectrum near the trailing-edge, provided by two distinct representative models reconstructing the wall-pressure spectra from RANS inputs: the deterministic YR model directly based on the integral parameters of the boundary layer and the PL statistical model based on the velocity field in the boundary layer.

In the airfoil case, the uncertainty is introduced as random velocity components at the inlet of a restricted computational domain, embedded in the jet potential core of the full anechoic wind tunnel. These random variables are intended to model the actual experimental uncertainty in the probe position and in the measurement of the reference velocity, and the numerical inaccuracies in the prediction of the jet development and deflection. To investigate the accuracy of the RANS based method, fully converged unsteady turbulent flow predictions are also provided by incompressible LES. Two deterministic incompressible flow solvers have then been coupled with a non-intrusive stochastic Galerkin method based on a SC to propagate these aerodynamic uncertainties. The flow topology associated with both types of simulations has revealed several noticeable differences. Only in the LES, at the lowest inlet flow angles, the laminar recirculation bubble at the leading edge disappears and a new one forms in the aft of the airfoil. The latter triggers an 8 dB increase in the wall-pressure spectra near the trailing edge. Such a flow bifurcation evidenced by LES could explain the noise increase of similar low-Reynolds number thin airfoils at low inlet flow angles and the noise increase of low-speed fans at high flow rates.[54] As a consequence, the LES-SC has larger uncertainty bars than the RANS-SC in the wall-pressure spectra and consequently in the far field noise over most frequencies. The RANS-UQ does not provide the good trend with incidence and misses the flow bifurcation and the shift of the recirculation bubble to the aft of the profile. When comparing both RANS-SC, both YR and PL models yield very small uncertainty bars around 1 kHz. The YR model has large increasing uncertainty bars at high frequencies caused by its strong dependence on the random wall shear-stress that has a broad probability density function and carries large uncertainties. On the contrary, the PL model has much smaller uncertainty bars at high frequencies but carries more uncertainty at the low frequencies caused by the slow convergence of the Monte Carlo technique used in this model.

In the fan case, realistic 5% and 4% errors about the mean are introduced on the volume flow-rate and the rotational speed respectively to account for the actual experimental and process scattering. The RANS

simulations of the fan mounted on a typical industrial test plenum have been run for each parameter yielding a total of 81 calculations. The resulting uncertainty bars obtained on the overall pressure rise match the experimental scattering quite well. By looking at the flow topology and particularly at the wall-pressure field, the variations are mainly located in the hub and the tip region under the fan rotating ring, resulting in large error bars on the corresponding wall-pressure spectra caused by the local flow separations. The final noise spectra of the complete fan are dominated in amplitude by the tip region while the uncertainty bars are related to uncertainties observed along the complete blade span. A proper control of the flow along the complete blade span is then necessary to reduce the uncertainties on the radiated sound. The uncertainties introduced by the variations on volume flow rate are much larger than those given by the rotational speed, and the combined effect of both fan parameters yield a 2-6 dB uncertainty on the far-field noise, with larger variations obtained with the YR model.

The convergence of the SC based on the RANS data set has been verified for both airfoil and fan cases by extending the number of terms in the Curtis-Clenshaw sparse quadrature and by comparing with a Monte Carlo simulation. In the airfoil case, the efficiency of the SC method is clearly demonstrated as it provides the same accuracy as the Monte Carlo approach with a limited number of terms (9) and is two orders of magnitude faster.

## Acknowledgements

The authors would like to thank Stanford University and Calcul Quebec (Compute Canada) for providing the necessary computational resources, and C. Hamman and G. Iaccarino for their support during the 2010 and 2012 CTR Summer Programs. This work was supported through the FP7-ECOQUEST project (Grant Agreement no 233541).

## References

1. S. Caro and S. Moreau, Aeroacoustic modeling of low pressure axial flow fans. In *6th AIAA/CEAS Aeroacoustics Conference* (2000). AIAA-2000-22094.
2. H. H. Hubbard and K. P. Shepherd, Aeroacoustics of large wind turbines, *J. Acoust. Soc. Am.* **89**(6), 2495–2508 (1991).
3. B. A. Singer, D. P. Lockard and K. S. Brentner, Computational aeroacoustic analysis of slat trailing-edge flow, *AIAA J.* **38**(9), 1558–1564 (2000).

4. S. Moreau, G. Iaccarino, S. Kang, Y. Khalighi and M. Wang, Numerical simulation of a low speed fan blade. In *Proceedings of the Summer Program 2004*, Centre for Turbulence Research, Stanford Univ./NASA Ames (2004).
5. S. Moreau, D. Neal, Y. Khalighi, M. Wang and G. Iaccarino, Validation of unstructured-mesh les of the trailing-edge flow and noise of a controlled-diffusion airfoil. In *Proceedings of the Summer Program 2006*, Centre for Turbulence Research, Stanford Univ./NASA Ames (2006).
6. J. Christophe, S. Moreau, C. Hamman, J. Witteveen and G. Iaccarino, Uncertainty quantification for the trailing-edge noise of a controlled-diffusion airfoil, *AIAA J.* **53**(1), 42–54 (2015).
7. Y. Addad, R. Prosser, D. Laurence, S. Moreau and F. Mendonca, On the use of embedded meshes in the les of external flow, *Flow Turbulence Combust.* **80**, 392–403 (2008).
8. M. Wang, S. Moreau and M. Roger, LES prediction of wall-pressure fluctuations and noise of a low-speed airfoil, *Internat. J. Aeroacoustics* **8**(3), 177–198 (2009).
9. J. Christophe, J. Anthoine and S. Moreau, Trailing edge noise of a controlled-diffusion airfoil at moderate and high angle of attack. In *15th AIAA/CEAS Aeroacoustics Conference* (2009). AIAA-2009-3196.
10. S. Moreau, M. Roger and J. Christophe, Flow features and self-noise of airfoils near stall or in stall. In *15th AIAA/CEAS Aeroacoustics Conference* (2009). AIAA-2009-3198.
11. J. Winkler, S. Moreau and T. Carolus, Large-eddy simulation and trailing-edge noise prediction of an airfoil with boundary-layer tripping. In *15th AIAA/CEAS Aeroacoustics Conference* (2009). AIAA-2009-3197.
12. L. Corriveau, S. Moreau, M. Roger and J. Christophe, Experimental and numerical unsteady acoustic sources and self-noise of a katana blade. In *16th AIAA/CEAS Aeroacoustics Conference* (2010). AIAA-2010-3804.
13. J. Winkler, T. Carolus and S. Moreau, Airfoil trailing-edge blowing: broadband noise prediction from large-eddy simulation, *AIAA J.* **50**(2), 1558–1564 (2012).
14. M. Sanjosé, S. Moreau, M. Kim and F. Pérot, Direct self-noise simulation of the installed controlled diffusion airfoil. In *17th AIAA/CEAS Aeroacoustics Conference* (2011). AIAA-2011-2716.
15. D. Casalino, S. Moreau and M. Roger, One, no one and one hundred thousand methods for low-speed fan noise prediction, *Internat. J. Aeroacoustics* **3**(3), 307–327 (2010).
16. S. Glegg, B. Morin, O. Atassi and R. Reba, Using Reynolds-averaged Navier–Stokes calculations to predict trailing edge noise, *AIAA J.* **48**(7), 1290–1301 (2010).
17. Y. Rozenberg, S. Moreau, M. Henner and S. C. Morris, Fan trailing-edge noise prediction using RANS simulations. In *16th AIAA/CEAS Aeroacoustics Conference* (2010). AIAA-2010-3720.
18. S. Remmler, J. Christophe, J. Anthoine and S. Moreau, Computation of wall-pressure spectra from steady flow data for noise prediction, *AIAA J.* **48**(9), 1997–2007 (2010).

19. J. Christophe, S. Moreau, C. Hamman, J. Witteveen and G. Iaccarino, Uncertainty quantification for the trailing-edge noise of a controlled-diffusion airfoil. In *Proceedings of the Summer Program 2010* (2010).
20. J. Christophe and S. Moreau, Uncertainty quantification of low-speed fan noise. In *Proceedings of the Summer Program 2012*, Centre for Turbulence Research, Stanford Univ./NASA Ames (2012).
21. W. Oberkampf, T. Trucano and C. Hirsch, Verification, validation and predictive capability in computational engineering and physics, *Appl. Mech. Rev.* **57**(5), 345–384 (2004).
22. R. H. Schlinker and R. K. Amiet, Helicopter rotor trailing edge noise. Technical Report. NASA CR 3470 (1981).
23. S. Moreau, M. Henner, G. Iaccarino, M. Wang and M. Roger, Analysis of flow conditions in freejet experiments for studying airfoil self-noise, *AIAA J.* **41**(10), 1895–1905 (2003).
24. R. L. Panton and J. H. Linebarger, Wall pressure spectra calculations for equilibrium boundary layers, *J. Fluid Mech.* **65**(02), 261–287 (1974).
25. J. Christophe, M. Sanjosé and S. Moreau, Uncertainty quantification of a low-speed axial fan self-noise. In *Proceedings ISROMAC Conference 2012* (2012).
26. M. Roger and S. Moreau, Back-scattering correction and further extensions of amiet's trailing-edge noise model. Part 1: theory, *J. Sound Vib.* **286**, 477–506 (2005).
27. R. Walters and L. Huyse, Uncertainty analysis for fluid mechanics with applications. Technical Report NASA CR-2002-211449 (2002).
28. D. Cacusi, *Sensitivity and Uncertainty Analysis*. CRC Press (2003).
29. D. Lucor, D. Xiu, C. Su and G. Karniadakis, Predictability and uncertainty in CFD, *Int. J. Numer. Methods Fluids* **43**(5), 483–505 (2003).
30. G. Iaccarino, Quantification of uncertainty in flow simulations using probabilistic methods, *VKI Lecture Series — Nonequilibrium Gas Dynamics* (2008).
31. H. N. Najm, Uncertainty quantification and polynomial chaos techniques in computational fluid dynamics, *Ann. Rev. Fluid Mech.* **41**, 35–52 (2009).
32. M. A. Tatang, W. Pan, R. G. Prinn and G. J. McRae, An efficient method for parametric uncertainty analysis of numerical geophysical models, *J. Geophys. Res.* **102**(D18), 21,925–21,922 (1997).
33. I. Babuska, F. Nobile and R. A. Tempone, A stochastic collocation method for elliptic partial differential equations with random input data, *SIAM J. Numer. Anal.* **45**(3), 1005–1034 (2007).
34. J. C. Chassaing and D. Lucor, Stochastic investigation of flows about airfoils at transonic speeds, *AIAA J.* **48**(5), 938–950 (2010).
35. C. W. Clenshaw and A. R. Curtis, A method for numerical integration on an automatic computer, *Numer. Math.* **2**, 197–205 (1960).
36. R. K. Amiet, Noise due to turbulent flow past a trailing edge, *J. Sound Vibration.* **47**(3), 387–393 (1976).
37. M. J. Lighthill, On sound generated aerodynamically. I. general theory, *Proc. R. Soc. L. Series A.* **211**(1102), 564–587 (1952).

38. S. Moreau and M. Roger, Competing broadband noise mechanisms in low-speed axial fans, *AIAA J.* **45**(1), 48–57 (2007).
39. S. Sinayoko, M. Kingan and A. Agarwal, Trailing edge noise theory for rotating blades in uniform flow, *Proc. R. Soc. A* **469**, 20130065 (2013).
40. D. Coles, The law of the wake in the turbulent boundary layers, *J. Fluid Mech.* **1**(2), 191–226 (1956).
41. Y. Rozenberg, *Modélisation analytique du bruit aérodynamique à large bande des machines tournantes: utilisation de calculs moyennés de mécanique des fluides,* PhD thesis, Ecole Centrale de Lyon (2007).
42. S. Moreau and M. Roger, Effect of airfoil aerodynamic loading on trailing-edge noise sources, *AIAA J.* **43**(1), 41–52 (2005).
43. S. Magne, M. Sanjosé, S. Moreau and A. Berry, Aeroacoustic prediction of the tonal noise radiated by a ring fan in uniform inlet flow. In *18th AIAA/CEAS Aeroacoustics Conference* (2012). AIAA-2012-2122.
44. F. Menter, Two-equation eddy viscosity turbulence models for engineering applications, *AIAA J.* **32**(8), 1598–1605 (1994).
45. M. Germano, U. Piomelli, P. Moin and W. H. Cabot, A dynamic subgrid-scale eddy viscosity model, *Phys. Fluids A* **3**(7), 1760–1765 (1991).
46. D. Lilly, A Proposed modification of the Germano Subgrid-Model Closure Method, *Phys. Fluids A* **4**(3), 633–635 (1992).
47. J. Kim and P. Moin, Application of a fractional-step method to incompressible Navier–Stokes equations, *J. Comput. Phys.* **59**, 308–323 (1985).
48. K. Mahesh, G. Constantinescu and P. Moin, A numerical method for large-eddy simulation in complex geometries, *J. Comput. Phys.* **197**, 215–240 (2004).
49. F. Ham and G. Iaccarino, Energy conservation in collocated discretization schemes on unstructured meshes. In *Annual Research Briefs*, Centre for Turbulence Research, Stanford Univ./NASA Ames (2004).
50. P. Sagaut, *Large Eddy Simulation for Incompressible Flows.* Springer-Verlag (2002).
51. T. Sayadi and P. Moin, Predicting natural transition using large eddy simulation. In *Annual Research Briefs*, Centre for Turbulence Research, Stanford Univ./NASA Ames (2011).
52. S. Moreau, M. Sanjosé, S. Magne and M. Henner, Aerocoustic predictions of a low-subsonic axial fan. In *Proceedings ISROMAC Conference 2012* (2012).
53. M. Sanjosé, D. Lallier-Daniels and S. Moreau, Aeroacoustics analysis of a low subsonic axial fan. In *ASME Turbo Expo 2015 Conference*, number ASME GT2015-12345, Montreal, Canada (June 15–19, 2015).
54. R. E. Longhouse, Noise separation and design considerations for low tip-speed and axial-flow fans, *J. Sound Vibration.* **4**(48), 461–474 (1976).